# Increased sky coverage with optimal correction of tilt and tilt-anisoplanatism modes in laser-guide-star multiconjugate adaptive optics

**Carlos Correia,[1,*] Jean-Pierre Véran,[1] Glen Herriot,[1] Brent Ellerbroek,[2] Lianqi Wang,[2] and Luc Gilles[2]**

[1]*National Research Council, Herzberg Institute of Astrophysics, 5071 W. Saanich Rd., Victoria, British Columbia V9E 2E7, Canada*
[2]*Thirty Meter Telescope Observatory Corporation, 1200 East California Boulevard, MC 102-8, Pasadena, California 91125, USA*
**Corresponding author: ccorreia@uvic.ca*

Received December 6, 2012; revised January 25, 2013; accepted January 25, 2013; posted January 29, 2013 (Doc. ID 181273); published March 11, 2013

Laser-guide-star multiconjugate adaptive optics (MCAO) systems require natural guide stars (NGS) to measure tilt and tilt-anisoplanatism modes. Making optimal use of the limited number of photons coming from such, generally dim, sources is mandatory to obtain reasonable sky coverage, i.e., the probability of finding asterisms amenable to NGS wavefront (WF) sensing for a predefined WF error budget. This paper presents a Strehl-optimal (minimum residual variance) spatiotemporal reconstructor merging principles of modal atmospheric tomography and optimal stochastic control theory. Simulations of NFIRAOS, the first light MCAO system for the thirty-meter telescope, using ~500 typical NGS asterisms, show that the minimum-variance (MV) controller delivers outstanding results, in particular for cases with relatively dim stars (down to magnitude 22 in the H-band), for which low-temporal frame rates (as low as 16 Hz) are required to integrate enough flux. Over all the cases tested ~21 nm rms median improvement in WF error can be achieved with the MV compared to the current baseline, a type-II controller based on a double integrator. This means that for a given level of tolerable residual WF error, the sky coverage is increased by roughly 10%, a quite significant figure. The improvement goes up to more than 20% when compared with a traditional single-integrator controller. 

*OCIS codes:* 010.1080, 000.5490, 110.6960.

## 1. TILT-ANISOPLANATISM IN LASER-TOMOGRAPHY ADAPTIVE-OPTICS SYSTEMS

### A. Adaptive Optics, Tomography, and Multiconjugate Adaptive Optics

Atmospheric turbulence is a major factor limiting the angular resolution achievable from ground-based telescopes [1,2] when observing at optical and near-infrared (NIR) wavelengths. Adaptive-optics (AO) systems partially overcome this effect: a basic AO system consists of a deformable mirror (DM) whose shape is adapted in real time to correct for the wavefront (WF) distortions induced by the turbulence, based on measurements provided by a WF sensor (WFS) looking at a guide source (guide star).

However, the correction patch is limited by angular anisoplanatism; i.e., the correction degrades away from the sensing direction where the WFS probe is located, leading to small corrected fields. Significantly larger fields can be obtained by correcting for the WF with several DMs (instead of a single one), each optically conjugated to a different altitude in the atmosphere. Such an AO system is called multiconjugate AO (MCAO) [3]. Several WFSs are used to measure the three-dimensional atmospheric disturbances projected at different angles. These measurements are then utilized to estimate the WF distortions on a discrete number of layers based on *a priori* second-order spatial moments of the WF disturbance and the measurement noise for which relatively accurate physical models exist [4]. Such algorithms are called *minimum-variance* (MV) since they minimize the residual pupil-integrated phase-variance cost functional—equivalently they optimize the Strehl ratio (SR) [5]—and do not take any temporal correlation into account. Once the tomographic or volumetric estimation of the WF above the observatory is available, the phase estimates are linearly projected onto (>1) DMs to minimize the residual in a given field of view (FoV). MCAO consists thus of a sequential combination of multiconjugation with atmospheric tomography.

The need to find several guide stars bright enough and close enough to the science field to make tomographic reconstruction possible renders natural guide star (NGS)-based MCAO impractical. Only one NGS MCAO system has been developed, with the main purpose of demonstrating the MCAO concept, but it is limited to few science cases [6].

### B. Tip/Tilt/Focus Uncertainty in Laser-Assisted AO

Even on future generation, 30–40 m class *Extremely Large Telescopes* (ELTs), using only NGSs to drive the AO systems, would reach very small portions of the available sky. Most AO systems will use laser-guide-stars (LGSs) in order to achieve scientifically useful levels of sky coverage for astronomical MCAO systems. LGSs produce a beacon high in Earth's atmosphere whose backscattered light is collected to probe a conical-shaped volume and compute WF distortions. Sodium LGSs are tuned to a resonance line located at 589 nm

 

wavelength. These then cause sodium to fluoresce in the mesosphere at around 90 km.

Due to tubulence-induced jitter in the upward propagation of the laser beam, the position of an LGS is uncertain, and therefore WF tilt errors cannot be determined from an LGS WFS. In an AO tomography context, the tilt indetermination on each LGS WFS translates into an inability to determine both global tip and tilt and field-dependent tilt, called tilt-anisoplanatism (TA) [7]. TA can be modeled by a combination of quadratic WF aberrations at two or more ranges that produce field-dependent tip-tilt (TT), canceling out in each LGS WFS, except for tilt, which is not sensed. These modes lead to plate-scale errors in the final science image. They are thus also referred to *plate-scale* modes.

In LGS-MCAO systems, mesospheric sodium-range variations provoke an additional focus error term, as the LGS are suddenly and temporarily out of focus. This term adds up indirectly to the atmospheric focus error, since the DMs are quickly driven to supersede such range mismatch, thus being seen in closed loop by the NGS WFS as focus error. Subsequently, based on the NGS modes' measurements, a temporal filtering loop offloads slow-varying range variations to a trombone focused at the mean altitude of the sodium layer. On longer time scales, the LGS WFS's centroiding algorithms based on matched filters are updated to further take such effects into account.

### C. Sky Coverage

Sky coverage is defined here as *the probability of finding a suitable asterism for NGS modes sensing within the allowable patrol field under a tolerable residual WF error* [8].

To sense TT, TA, and focus modes, a set of several NGSs is used with varying limiting magnitudes. High sky-coverage goals will require dim NGSs, which implies increasing the exposure times to integrate sufficient light flux [9,10]. Therefore, the NGS loops may run at low frame rates (few tens of hertz) even with the light-gathering capacity of the ELTs. The temporal controller used for the NGS modes is commonly an integrator with optimized gain, but this is recognizably far from optimal and can thus be further improved.

High gains in sky coverage can potentially be achieved by using more efficient temporal controllers. In this paper the Strehl-optimal MV spatiotemporal controller is presented. The MV controller can further take advantage of the multiple control loop frame rates required by laser-tomographic systems combining LGS and NGS measurements by interpolating (smoothing) the correction.

### D. Current and Future Instruments

To date, there has been only one LGS-MCAO system that has worked on sky: GeMS at the 8 m Gemini-south telescope [11,12]. However, large-scale efforts are underway to design MCAO systems for the next generation of ELTs, which will have a diameter between 20 and 40 m. These include MAORY for the European ELT (E-ELT) [13] and the first light NFIRAOS for the thirty-meter telescope (TMT) [14,15]. Although not currently under design, a MCAO system for the giant magellan telescope (GMT) is not precluded [16].

NFIRAOS has two DMs conjugated to 0 and 11.2 km above the telescope, respectively, and six LGS WFSs, with one on-axis plus five more arranged in a 35 arc sec radius pentagon. Sensing of global TT, TA, and residual focus is possible thanks to two NIR (J, H, and Ks bands) single-aperture tilt sensors and one $2 \times 2$ Shack–Hartmann WFS, sensing tip, tilt, focus, and astigmatism (TTFA). These are on-instrument WFSs (OIWFSs) because instead of being located in the AO system, they are located in the science instrument IRIS, the infrared imager and spectrograph [17].

NFIRAOS LGS WFSs will run at a frame rate of 800 Hz, but the OIWFSs are expected to run at 20–800 Hz, depending on the brightness of the NGSs. The 50% sky-coverage goal at the galactic pole, where the NGS density is the lowest, led to a median frame rate around 90 Hz [18]. In this case, guide stars as dim as magnitude 22 in the H-band are used to correct for TT and TA modes.

The MV controller proposed here fits on the framework of *ad hoc split tomography* (AHST), in which the LGS and NGS correction loops are driven independently—adopted as the baseline option for NFIRAOS [19]. Such a scheme is known to be suboptimal, which led to a joint estimate of the NGS + LGS modes in the so called *minimum-variance split tomography* (MVST) scheme [20,21]. Although both suffer from an approximate forward model relying on pseudo-open-loop measurements to comply with closed-loop operation, the latter delivers better results by taking into account high-order aliasing on the NGS modes, in particular for off-zenith observations and with multiobject AO systems. Taking one step back, AHST is conceptually less complex, and it is computationally less demanding and easier to implement. The optimality referred to in this paper has thus to be understood under AHST and is specific for the six NGS modes that are taken into account here and not the full tomographic reconstruction and closed-loop control. In a future step, the results presented here should be extended to MVST.

Optimizing the NGS controller can, however, improve performance and sky coverage. Earlier systems such as GeMS use integral controllers for each NGS mode, with gains adjusted as a function of signal-to-noise ratio on the NGS WFSs. For NFIRAOS, a more complex type-II controller based on a double integrator and a lead filter has been proposed [22], and adopted as baseline [18]. In this paper, the NGS processing takes one step further: an MV formulation is presented taking advantage of the spatiotemporal correlation between the different NGS modes, as well as making optimal use of the multiple control loop frame rates, which occur in LGS-MCAO systems.

This document is organized as follows. Section 2 details the linear modeling of the NGS modes and the measurement models. Section 3 presents the MV problem and provides a dynamic solution using the *linear-quadratic-Gaussian* (LQG) framework. In Section 4 sample numerical results are provided to illustrate the advantages of this enhanced MV controller, compared to the suboptimal approaches that have been proposed previously. Section 5 concludes this work.

## 2. LINEAR MODELING OF TT/TA AND FOCUS MODES

For a two-DM-MCAO system like the TMT NFIRAOS, five modes representing global TT modes and the three dominant TA modes causing image magnification and differential

magnification at 0 and 45 deg carry more than 80% of the total error variance in the NGS modes [9,10]. The latter can be corrected for by applying a combination of three quadratic modes (focus and astigmatism) with proportional amplitudes in two conjugate planes [23].

The total aperture-plane WF error induced by the TT/TA modes at time instant $t$, in direction $\boldsymbol{\theta}$, is given by

$$W(\boldsymbol{\rho},\boldsymbol{\theta},t)=\sum_{i=2}^{6}\alpha_i(t)Z_i\left(\frac{\boldsymbol{\rho}}{R_0}\right)+\sum_{i=2}^{6}\beta_i(t)Z_i\left(\frac{\boldsymbol{\rho}+\boldsymbol{\theta}h_{\mathrm{DM11.2}}}{R_h}\right), \tag{1}$$

where $\boldsymbol{\rho}$ is a two-dimensional space coordinate vector and $\boldsymbol{\alpha}$ and $\boldsymbol{\beta}$ are vectors containing the Zernike coefficients (following the ordering of [24]) defined over the lower and upper DM-conjugate planes of radius $R_0=D_0/2$ and $R_h=D_h/2$; see Fig. 1. Note $i\in\{2,\cdots,6\}$, which effectively represents five modes; $i=1$ refers to piston and is disregarded as this mode has no impact on AO performance. Global TT has the corresponding Zernike modes applied to the ground DM only; i.e., $\beta_2=\beta_3=0$.

The coefficients $\beta_i$ can be worked out such that $W(\boldsymbol{\rho},\boldsymbol{\theta},t)$ only produces TT in the LGS WFSs (but not on the NGS WFSs). This constraint provides $\beta_i=-r_l^{-2}\alpha_i$, with $r_l$ given by the ratio of diameters of the cone-intersected pupil and the DM11.2 meta-pupil (see Fig. 1 for a visual depiction), i.e.,

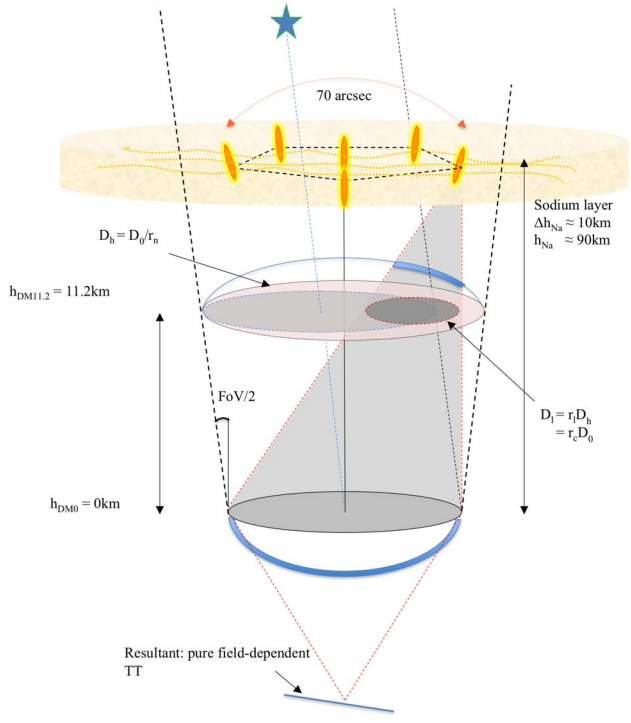


Fig. 1. (Color online) NGS modes diagram. The TA modes each contain a quadratic Zernike polynomial with proportional amplitudes on the ground and upper DMs, whose combined effect produces pure TT in the LGS WFSs (thus not sensed), but contains field-dependent TT (plate-scale effect) and quadratic WF aberrations across the science field and NGS patrol field.

$$r_l=r_n\underbrace{\left(1-\frac{h_{\mathrm{DM11.2}}}{h_{\mathrm{Na}}}\right)}_{r_c}, \tag{2}$$

where $r_c\triangleq 1-h_{\mathrm{DM11.2}}/h_{\mathrm{Na}}$ is the shrinking factor of the cone-intersected meta-pupil diameter with respect to the cylinder-intersected meta-pupil diameter at $h_{\mathrm{DM11.2}}=11.2$ km, translating the cone effect for a DM conjugated to range $h_{\mathrm{DM11.2}}$ and an LGS at range $h_{\mathrm{Na}}$ (see Fig. 1), and

$$r_n\triangleq\frac{D_0}{D_0+FoV\times h_{\mathrm{DM11.2}}\times 1000}, \tag{3}$$

normalizes the upper modal coefficient to the particular choice of underlying meta-pupils over which the modes are defined, with $FoV$ the field of view in radians, and $h_{\mathrm{DM11.2}}$ the conjugate altitude of the upper DM in kilometers.

Although the NGS modes produce only field-dependent TT not seen by the LGS WFS, for an NGS looking upward through a cylinder and not a cone, focus and astigmatism are indeed probed.

The varying altitude of the sodium layer induces a focus error term that must also be measured using the NGS stars. These variations are given by [25]

$$\sigma_{\mathrm{Na}}=\frac{D_0^2}{16\sqrt{3}h^2}\Delta h\quad[\mathrm{m\,rms}], \tag{4}$$

with $\Delta h=31$ m$^2$/Hz at 1 Hz.

### A. Low-Order Tomographic Geometrical Model for TT/TA and Focus Modes

Following Eq. (1), the resulting aperture-plane WF $W(\boldsymbol{\rho},\boldsymbol{\theta},t)$ is conveniently expanded onto a truncated orthonormal Zernike polynomial's basis defined over two layers. For the NGS modes model, only modes $Z_{2\cdots6}$ are used that correspond to the TT and the quadratic modes of Eq. (1).

Setting $\beta_i=-r_l^{-2}\alpha_i$ in Eq. (1) and solving for the aperture-plane field-dependent TT,

$$W_{\mathrm{TT}}(\boldsymbol{\rho},\boldsymbol{\theta},t)=\sum_{i=2}^{3}\xi_i(\theta,t)Z_i\left(\frac{\boldsymbol{\rho}}{R_0}\right), \tag{5}$$

with the field-dependent TT coefficients $\xi(\boldsymbol{\theta},t)$ [7],

$$\xi(\boldsymbol{\theta},t)=\begin{pmatrix}1 & 0 & -r_c^{-2}\frac{2\sqrt{3}h\theta_x}{R_0} & -r_c^{-2}\frac{\sqrt{6}h\theta_y}{R_0} & -r_c^{-2}\frac{\sqrt{6}h\theta_x}{R_0} & 0\\ 0 & 1 & -r_c^{-2}\frac{2\sqrt{3}h\theta_y}{R_0} & -r_c^{-2}\frac{\sqrt{6}h\theta_x}{R_0} & r_c^{-2}\frac{\sqrt{6}h\theta_y}{R_0} & 0\end{pmatrix}\boldsymbol{\mu}(t). \tag{6}$$

In Eq. (6) $\boldsymbol{\mu}(t)\in\Re^{6\times1}$ is a vector with the coefficient of the NGS modes [numerically equal to $\boldsymbol{\alpha}(t)$ in Eq. (1) but not to be confounded with it] plus a sixth coefficient to model pure focus induced by the $N_a$ layer that does not produce TT.

Since one is interested in measuring also focus and astigmatism with the $2\times2$ subaperture TTFA WFS, the model of Eq. (6) needs to be expanded beyond TT. It will be carried out in two steps, making explicit use of the layered modal decomposition of the WF error: (1) a linear modal projection

of modes from layers in the aperture and (2) linear relation of NGS mode coefficients to their layered counterparts.

By separating the layer contributors to the total WF, the Zernike polynomials' coefficients are gathered in the vector $\boldsymbol{\varphi} \in \Re^{10\times 1}$

$$\boldsymbol{\varphi}(t) \triangleq \begin{bmatrix} \boldsymbol{\alpha} \\ \boldsymbol{\beta} \end{bmatrix}(t), \tag{7}$$

which concatenates WF coefficients of the decomposition of the WF phase at the two DM-conjugate altitudes. The Zernike polynomials are defined over a pupil of diameter $D_0$ on the ground and $D_{\mathrm{DM11.2}} = D_0/r_n$ for the upper conjugate layer; i.e., $D_{\mathrm{DM11.2}} > D_0$ since $r_n < 1$, as depicted in Fig. 1.

Using the fundamentals of modal tomography modeling [26], the aperture-plane WF decomposition $\boldsymbol{\phi}(\boldsymbol{\theta}, t)$ relates to the layered decomposition by a linear projection

$$\boldsymbol{\phi}(\boldsymbol{\theta}, t) = \mathbf{P}_{\theta}\boldsymbol{\varphi}(t), \tag{8}$$

with $\mathbf{P}_{\theta} \in \mathbb{R}^{9\times 10}$ a projection matrix of Zernike polynomials onto the intersected meta-pupils in DM-conjugated planes with a pupil-sized cylinder of diameter $D_0$ in the directions $\boldsymbol{\theta}$ of the NGS. Therefore, concatenating the angular linear projectors for the two single-aperture TT and the TTFA OIWFS directions, one gets

$$\mathbf{P}_{\theta}(\boldsymbol{\theta}) \triangleq \begin{pmatrix} \mathbf{P}_{\theta,\mathrm{TT1}}(\boldsymbol{\theta}) \\ \mathbf{P}_{\theta,\mathrm{TT2}}(\boldsymbol{\theta}) \\ \mathbf{P}_{\theta,\mathrm{TTFA}}(\boldsymbol{\theta}) \end{pmatrix} \times \begin{pmatrix} 1 & 0 & 0 & 0 & 0 & r_n & 0 & p_{1,8} & p_{1,9} & p_{1,10} \\ 0 & 1 & 0 & 0 & 0 & 0 & r_n & p_{2,8} & p_{2,9} & p_{2,10} \\ 1 & 0 & 0 & 0 & 0 & r_n & 0 & p_{3,8} & p_{3,9} & p_{3,10} \\ 0 & 1 & 0 & 0 & 0 & 0 & r_n & p_{4,8} & p_{4,9} & p_{4,10} \\ 1 & 0 & 0 & 0 & 0 & r_n & 0 & p_{5,8} & p_{5,9} & p_{5,10} \\ 0 & 1 & 0 & 0 & 0 & 0 & r_n & p_{6,8} & p_{6,9} & p_{6,10} \\ 0 & 0 & 1 & 0 & 0 & 0 & 0 & r_n^2 & 0 & 0 \\ 0 & 0 & 0 & 1 & 0 & 0 & 0 & 0 & r_n^2 & 0 \\ 0 & 0 & 0 & 0 & 1 & 0 & 0 & 0 & 0 & r_n^2 \end{pmatrix}, \tag{9}$$

where the left-column block of $\mathbf{P}_{\theta}$ is composed by identity blocks since the ground DM is conjugated to 0 km. The coefficients $p_{m,n}$ are asterism-dependent coefficients found from clipping the upper meta-pupil in $D_0$-sized patches and recasting the coefficient as a linear combination of modes defined over the ground pupil. The analytical procedure is given in Eq. (6) for TT, and a generalization to any mode can be found in [27]. Dashed lines subdivide the matrix $\mathbf{P}_{\theta}$ into three horizontal slabs for the three OIWFS and two vertical slabs, for the two DM-conjugate altitudes.

The relation of Zernike polynomial coefficients $\boldsymbol{\varphi}(t)$ to NGS mode coefficients $\boldsymbol{\mu}(t)$ is given in matrix format

$$\boldsymbol{\varphi}(t) \triangleq \mathbf{P}_{\mu 2\varphi}\boldsymbol{\mu}(t), \tag{10}$$

where $\mathbf{P}_{\mu 2\varphi} \in \mathbb{R}^{10\times 6}$ translates six NGS mode coefficients to their layered version expressed in Zernike polynomials. Hence

$$\mathbf{P}_{\mu 2\varphi} \triangleq \begin{pmatrix} 1 & 0 & 0 & 0 & 0 & 0 \\ 0 & 1 & 0 & 0 & 0 & 0 \\ 0 & 0 & 1 & 0 & 0 & 1 \\ 0 & 0 & 0 & 1 & 0 & 0 \\ 0 & 0 & 0 & 0 & 1 & 0 \\ 0 & 0 & 0 & 0 & 0 & 0 \\ 0 & 0 & 0 & 0 & 0 & 0 \\ 0 & 0 & -1/r_l^2 & 0 & 0 & 0 \\ 0 & 0 & 0 & -1/r_l^2 & 0 & 0 \\ 0 & 0 & 0 & 0 & -1/r_l^2 & 0 \end{pmatrix}. \tag{11}$$

Note the last column corresponds to the pure focus mode induced by sodium-range variations on the ground layer.

It can be checked that the product $\mathbf{P}_{\theta}\mathbf{P}_{\mu 2\varphi}$ is equal to Eq. (5) for the TT modes in any direction.

### B. Measurement Model

Assume the following measurement model:

$$\boldsymbol{s}_k = \int_{(k-1)T_s}^{kT_s} \mathbf{G}(\mathbf{P}_{\theta}\boldsymbol{\varphi}(\tau)^{-}\mathbf{P}_{\theta}\boldsymbol{\varphi}^{\mathrm{dm}}(\tau))\mathrm{d}\tau + \boldsymbol{\eta}_k \tag{12a}$$

$$= \mathbf{G}\mathbf{P}_{\theta}(\langle\boldsymbol{\varphi}\rangle_k - \langle\boldsymbol{\varphi}^{\mathrm{dm}}\rangle_k) + \boldsymbol{\eta}_k \tag{12b}$$

$$= \mathbf{G}\mathbf{P}_{\theta}\langle\boldsymbol{\varphi}^{\mathrm{res}}\rangle_k + \boldsymbol{\eta}_k, \tag{12c}$$

where $\boldsymbol{s}_k \in \Re^{12\times 1}$ are the $T_s$-averaged slopes over each OIWFS subaperture and over the integration time $T_s$, $\mathbf{G} \in \mathbb{R}^{12\times 9}$ is the WF-to-measurement matrix, "dm" and "res" stand, respectively, for correction and residual phase, $\boldsymbol{\eta}_k$ is a zero-mean Gaussian-distributed spectrally white-noise vector with known covariance matrix $\sum_{\eta} -\boldsymbol{\eta} \sim \mathcal{N}(0, \Sigma_{\eta})$— and $\mathbf{P}_{\theta}$ is defined in Eq. (9).

The symbol $\langle\cdot\rangle$ represents the time average, i.e.,

$$\langle\boldsymbol{\varphi}\rangle_k \triangleq \int_{(k-1)T_s}^{kT_s} \boldsymbol{\varphi}(\tau)\mathrm{d}\tau. \tag{13}$$

Define $\mathbf{P}_{\mathrm{NGS}} \in \Re^{9\times 6}$ as

$$\mathbf{P}_{\mathrm{NGS}} = \mathbf{P}_{\theta}\mathbf{P}_{\mu 2\varphi}, \tag{14}$$

the projection of NGS modes onto TT and quadratic Zernike polynomials, the modes to be measured by the three OIWFSs. Consequently, Eq. (12) can be rewritten as follows:

$$\boldsymbol{s}_k = \mathbf{G}(\mathbf{P}_{\mathrm{NGS}}\langle\boldsymbol{\mu}\rangle_k - \mathbf{P}_{\mathrm{NGS}}\langle\boldsymbol{\mu}^{\mathrm{dm}}\rangle_k) + \boldsymbol{\eta}_k, \tag{15}$$

with the NGS modes

$$\langle\boldsymbol{\mu}\rangle_k \triangleq \mathbf{P}_{\mu 2\varphi}^{\dagger}\langle\boldsymbol{\varphi}\rangle_k, \tag{16a}$$

$$\langle\boldsymbol{\mu}^{\mathrm{dm}}\rangle_k \triangleq \mathbf{P}_{\mu 2\varphi}^{\dagger}\langle\boldsymbol{\varphi}^{\mathrm{dm}}\rangle_k, \tag{16b}$$

and $\mathbf{P}_{\mu 2\varphi}^{\dagger}$ the generalized inverse of matrix $\mathbf{P}_{\mu 2\varphi}$ in Eq. (11).

The correction phase applied by the DM is $\langle\boldsymbol{\varphi}^{\mathrm{dm}}\rangle_k \triangleq \mathbf{N}\boldsymbol{u}_{k-1}$ with $\mathbf{N}\in\mathbb{R}^{10\times10}$ the command-to-phase matrix and with $\boldsymbol{u}_{k-1}\in\Re^{10\times1}$ the DM commands.

The modal matrix $\mathbf{G}$ translates modal coefficients of TT, TT and TTFA modes into average slopes over the illuminated subregion of each subaperture

$$\mathbf{G}\triangleq\begin{pmatrix}\mathbf{G}_{\mathrm{TT1}}\\ \mathbf{G}_{\mathrm{TT2}}\\ \mathbf{G}_{\mathrm{TTFA}}\end{pmatrix}=\begin{pmatrix}\gamma_{\mathrm{T}} & 0 & 0 & 0 & 0 & 0 & 0 & 0 & 0\\ 0 & \gamma_{\mathrm{T}} & 0 & 0 & 0 & 0 & 0 & 0 & 0\\ 0 & 0 & \gamma_{\mathrm{T}} & 0 & 0 & 0 & 0 & 0 & 0\\ 0 & 0 & 0 & \gamma_{\mathrm{T}} & 0 & 0 & 0 & 0 & 0\\ 0 & 0 & 0 & 0 & \gamma_{\mathrm{T}} & 0 & \gamma_{\mathrm{F}} & \gamma_{\mathrm{A}} & \gamma_{\mathrm{A}}\\ 0 & 0 & 0 & 0 & 0 & \gamma_{\mathrm{T}} & \gamma_{\mathrm{F}} & \gamma_{\mathrm{A}} & -\gamma_{\mathrm{A}}\\ 0 & 0 & 0 & 0 & \gamma_{\mathrm{T}} & 0 & -\gamma_{\mathrm{F}} & \gamma_{\mathrm{A}} & -\gamma_{\mathrm{A}}\\ 0 & 0 & 0 & 0 & 0 & \gamma_{\mathrm{T}} & \gamma_{\mathrm{F}} & -\gamma_{\mathrm{A}} & -\gamma_{\mathrm{A}}\\ 0 & 0 & 0 & 0 & \gamma_{\mathrm{T}} & 0 & -\gamma_{\mathrm{F}} & -\gamma_{\mathrm{A}} & \gamma_{\mathrm{A}}\\ 0 & 0 & 0 & 0 & 0 & \gamma_{\mathrm{T}} & -\gamma_{\mathrm{F}} & -\gamma_{\mathrm{A}} & \gamma_{\mathrm{A}}\\ 0 & 0 & 0 & 0 & \gamma_{\mathrm{T}} & 0 & \gamma_{\mathrm{F}} & -\gamma_{\mathrm{A}} & \gamma_{\mathrm{A}}\\ 0 & 0 & 0 & 0 & 0 & \gamma_{\mathrm{T}} & -\gamma_{\mathrm{F}} & \gamma_{\mathrm{A}} & \gamma_{\mathrm{A}}\end{pmatrix}. \tag{17}$$

For the TTFA OIWFS, the average slope produced by the TT on the quarter of the aperture $S_{(1/4)}=\pi/4$ (aperture units are normalized by the aperture radius) is given by

$$\gamma_{\mathrm{T}}=\frac{1}{S_{\frac{1}{4}}}\int_0^1\int_0^{\sqrt{1-y^2}}\frac{\partial}{\partial x}Z_{2,3}(x,y)\partial x\partial y=2. \tag{18}$$

The average slope produced by the focus mode is given by

$$\gamma_{\mathrm{F}}=\frac{1}{S_{\frac{1}{4}}}\int_0^1\int_0^{\sqrt{1-y^2}}\frac{\partial}{\partial x}Z_4(x,y)\partial x\partial y=\frac{16\sqrt{3}}{3\pi}, \tag{19}$$

whereas for the astigmatisms

$$\gamma_{\mathrm{A}}=\frac{1}{S_{\frac{1}{4}}}\int_0^1\int_0^{\sqrt{1-y^2}}\frac{\partial}{\partial x}Z_{5\cdots6}(x,y)\partial x\partial y=\frac{8\sqrt{6}}{3\pi}. \tag{20}$$

The symbol $\pm$ attached to $\gamma_{\mathrm{F}}$, and $\gamma_{\mathrm{A}}$ in Eq. (17) is a function of the exact quadrant where each subaperture is located.

Noise added to measurements follows formulae for TT in a quadrant detector found in [9,28]. When fewer than three NGSs are available within the 2 arc min patrol field, matrix $\mathbf{G}$ in Eq. (17) is truncated to account for the existing number of NGSs. In such cases, TTFA sensing is always performed.

## 3. STREHL-OPTIMAL RECONSTRUCTION AND CLOSED-LOOP CONTROL

### A. Merit Function: Minimum Pupil-Integrated Residual Phase Variance

In what follows, the minimization of the pupil-integrated mean-square residual phase after AO correction is considered. Minimizing the variance of $W^{\mathrm{res}}$ results in the maximization of the SR [5], leading to the continuous-time criterion

$$J^c(\boldsymbol{u})\triangleq\lim_{\tau\to+\infty}\frac{1}{\tau}\int_0^\tau\langle\|\boldsymbol{\phi}^{\mathrm{res}}(\boldsymbol{\theta},t)\|^2_{L_2(\Omega)}\rangle_{\theta_{\mathrm{sci}}}\mathrm{d}t, \tag{21}$$

$$=\lim_{\tau\to+\infty}\frac{1}{\tau}\int_0^\tau\langle\|\boldsymbol{\phi}(\theta,t)-\boldsymbol{\phi}^{\mathrm{dm}}(\boldsymbol{\theta},t)\|^2_{L_2(\Omega)}\rangle_{\theta_{\mathrm{sci}}}\mathrm{d}t, \tag{22}$$

where $\boldsymbol{\phi}$ is the aperture-plane phase from Eq. (8), $\boldsymbol{\phi}^{\mathrm{res}}=\boldsymbol{\phi}-\boldsymbol{\phi}^{\mathrm{dm}}$ is the residual phase, $\|\cdot\|^2_{L_2(\Omega)}$ represents the Euclidean norm over the pupil with weighting function $\Omega(\boldsymbol{\rho})$ [4], and $\langle\cdots\rangle_{\theta_{\mathrm{sci}}}$ represents averaging over a discrete number of $\boldsymbol{\theta}_{\mathrm{sci}}$ directions that sample the science field.

Optimality is to be understood with respect to the direct model chosen where only six NGS modes are considered.

### B. Minimum-Variance Negative State-Feedback Controller

Using the LQG formulation [29], the optimal controller has the form

$$\boldsymbol{u}_k^{\mathrm{opt}}=\mathbf{F}_\varphi\langle\boldsymbol{\varphi}\rangle_{k+1}, \tag{23}$$

$$=\mathbf{F}\langle\boldsymbol{\mu}\rangle_{k+1}, \tag{24}$$

where $\mathbf{F}\triangleq\mathbf{F}_\varphi\mathbf{P}_{\mu2\varphi}$ is a fitting operator that optimizes the correction in the directions where the science targets are located.

Since no temporal DM dynamics are considered, the control Riccati equation reduces to an orthogonal projection onto the DM-spanned space with the fitting operator boiling down to a least-squares projection given by $\mathbf{F}_\varphi\triangleq(\mathbf{N}^{\mathrm{T}}\langle\mathbf{P}_{\boldsymbol{\theta}}^{\mathrm{T}}\mathbf{P}_{\boldsymbol{\theta}}\rangle_{\boldsymbol{\theta}_{\mathrm{sci}}}\mathbf{N})^{\dagger}\mathbf{N}^{\mathrm{T}}\langle\mathbf{P}_{\boldsymbol{\theta}}^{\mathrm{T}}\mathbf{P}_{\boldsymbol{\theta}}\rangle_{\boldsymbol{\theta}_{\mathrm{sci}}}$. With the DM commanded directly in Zernike polynomials (i.e., $\mathbf{N}$ is the identity matrix), and noting that the phase is defined at the DM-conjugate altitudes only, the angular dependence drops and the fitting operator simplifies to the identity [4], yielding

$$\boldsymbol{u}_k^{\mathrm{opt}}\triangleq\langle\boldsymbol{\varphi}\rangle_{k+1}=\mathbf{P}_{\mu2\varphi}\langle\boldsymbol{\mu}\rangle_{k+1}. \tag{25}$$

This assumption is also valid in practice, since DM fit to low-order Zernike polynomials is quasi-perfect.

The vector of coefficients $\langle\boldsymbol{\varphi}\rangle_{k+1}$ is to be estimated by a Kalman filter providing $\langle\hat{\boldsymbol{\varphi}}\rangle_{k+1|k}$, i.e., the conditional mean of the disturbance phase given the set of current and past measurements $\mathcal{S}_{k\cdots0}$.

### C. State-Space Modeling

Define the discrete-time state-space model

$$\boldsymbol{x}_{k+1}=\mathcal{A}\boldsymbol{x}_k+\mathcal{B}\boldsymbol{u}_k+\Gamma e_k, \tag{26a}$$

$$\boldsymbol{s}_k=\mathcal{C}\boldsymbol{x}_k+\mathcal{D}\boldsymbol{u}_k+\boldsymbol{\eta}_k, \tag{26b}$$

where $\{\mathcal{A},\mathcal{B},\mathcal{C},\mathcal{D},\Gamma\}$ are matrices that concatenate discrete-time linear models for each of the modes (TT and TT anisoplanatism) [Eq. (1)] plus pure focus; $\Sigma_\epsilon$ and $\Sigma_w$ are the covariance matrices of state noise and measurement noise, respectively.

In what follows, second-order models are used. These are characterized by an asymptotic power-spectral density (PSD)

at high frequencies $\propto f^{-4}$, which approximates well enough the PSDs of the TT/TA modes; see Fig. 4. For focus, a first-order model suffices.

The second-order model for an individual mode is given by

$$(\boldsymbol{x}_k)_i \triangleq \begin{pmatrix} d_{1,k} \\ d_{2,k} \\ \langle \mu \rangle_k \end{pmatrix}_i, \tag{27a}$$

$$\mathcal{A}_i \triangleq \begin{pmatrix} [e^{A_i T_s}] & 0 \\ \Xi_i & 0 \end{pmatrix}, \qquad \mathcal{B}_i \triangleq 0, \qquad \Gamma_i \triangleq \mathrm{I}. \tag{27b}$$

This discrete-time state-space model produces instantaneous values of the NGS modes and average deformations over the loop sampling interval $\langle \mu_i \rangle_k$ as follows [29].

Assuming an underlying continuous-time linear model (Roman capital fonts used)

$$\begin{pmatrix} \dot{d}_1 \\ \dot{d}_2 \end{pmatrix}(t) = A_i \begin{pmatrix} d_1 \\ d_2 \end{pmatrix}(t) + \Gamma_i \varepsilon(t), \tag{28a}$$

$$\mu_i(t) = C_i \begin{pmatrix} d_1 \\ d_2 \end{pmatrix}(t), \tag{28b}$$

with $\dot{d}(t)$ the first temporal derivative of $d(t)$, it is found that the average deformation over the interval $T_s$ can be obtained from the discretized state at instant "$k$" in Eq. (28) as

$$\langle \mu_i \rangle_{k+1} = \frac{1}{T_s} \int_{kT_s}^{(k+1)T_s} \mu_i(\tau) \mathrm{d}\tau = \Xi_i \begin{pmatrix} d_1 \\ d_2 \end{pmatrix}_k, \tag{29}$$

where

$$\Xi_i \triangleq \frac{1}{T_s} C_i (e^{A_i T_s} - I) A_i^{-1}. \tag{30}$$

The full model is hence a concatenation of individual models

$$\boldsymbol{x}_k \triangleq \begin{pmatrix} \boldsymbol{x}_k^{\mathrm{tip}} \\ \boldsymbol{x}_k^{\mathrm{tilt}} \\ \boldsymbol{x}_k^{\Delta \mathrm{F}} \\ \boldsymbol{x}_k^{\Delta \mathrm{A}_0} \\ \boldsymbol{x}_k^{\Delta \mathrm{A}_{45}} \\ \boldsymbol{x}_k^{\mathrm{foc}} \end{pmatrix}, \qquad \mathcal{A} \triangleq \begin{pmatrix} \mathcal{A}_{\mathrm{tip}} & 0 & \cdots & \cdots & 0 \\ 0 & \mathcal{A}_{\mathrm{tilt}} & \cdots & \cdots & 0 \\ 0 & \cdots & \ddots & \vdots & \vdots \\ 0 & \cdots & \ddots & \mathcal{A}_{\Delta \mathrm{A}_{45}} & \vdots \\ 0 & \cdots & \cdots & \cdots & \mathcal{A}_{\mathrm{foc}} \end{pmatrix}, \tag{31a}$$

$$\mathcal{B} \triangleq \begin{pmatrix} \mathcal{B}_{\mathrm{tip}} \\ \mathcal{B}_{\mathrm{tilt}} \\ \vdots \\ \mathcal{B}_{\mathrm{foc}} \end{pmatrix}, \qquad \Gamma \triangleq \begin{pmatrix} \Gamma_{\mathrm{tip}} & 0 & \cdots & \cdots & 0 \\ 0 & \Gamma_{\mathrm{tilt}} & \cdots & \cdots & 0 \\ 0 & \cdots & \ddots & \vdots & \vdots \\ 0 & \cdots & \ddots & \Gamma_{\Delta \mathrm{A}_{45}} & \vdots \\ 0 & \cdots & \cdots & \cdots & \Gamma_{\mathrm{foc}} \end{pmatrix}, \tag{31b}$$

$$\mathcal{C} \triangleq \mathbf{G}\mathbf{P}_{\mathrm{NGS}}\mathbf{M}_{\mu}, \qquad \mathcal{D} \triangleq -z^{-1}\mathbf{G}\mathbf{P}_{\theta}\mathbf{N}. \tag{31c}$$

Variable $z^{-1}$ is the discrete backward time-shift operator.

For compactness reasons, for this particular choice of the state vector components in Eq. (27a), the one-step ahead average predicted disturbance is $\langle \hat{\boldsymbol{\mu}} \rangle_{k+1|k} \triangleq \mathbf{M}_{\mu} \mathcal{A} \hat{\boldsymbol{x}}_{k|k}$, where $\hat{\boldsymbol{x}}_{k|k}$ is the conditional expectation of the state $\boldsymbol{x}_k$ estimated by a Kalman filter using information $\mathcal{S}_{k \cdots 0}$, i.e., using the set of all past measurements up to time step "$k$," and where $\mathbf{M}_{\mu}$ is a 0–1 valued matrix that extracts the component $\langle \boldsymbol{\mu} \rangle_k$, i.e., the average TT/TA mode over $T_s$.

The Kalman filter is seamlessly obtained from an estimation Riccati equation. Since the metric of interest in AO is the long-exposure integration of light on the science instruments such that $T_{\mathrm{LE}} \gg T_s$, the asymptotic solution can be used with strictly no loss of performance. Under the assumption that a linear state-space model is built producing as outputs $\langle \hat{\boldsymbol{\varphi}} \rangle$ (see below), the optimal gains are computed offline from

$$\mathcal{L}_{\infty} = \mathcal{A}\mathcal{H}_{\infty} = \mathcal{A}\Sigma_{\infty}\mathcal{C}^{\mathrm{T}}(\mathcal{C}\Sigma_{\infty}\mathcal{C}^{\mathrm{T}} + \Sigma_w)^{-1}, \tag{32}$$

where $\mathcal{L}_{\infty}$ is the asymptotic Kalman gain, $\Sigma_{\infty}$ is the estimation error covariance matrix, and the solution of the algebraic Riccati equation is

$$\Sigma_{\infty} = \mathcal{A}\Sigma_{\infty}\mathcal{A}^{\mathrm{T}} + \Sigma_{\varepsilon} - \mathcal{A}\Sigma_{\infty}\mathcal{C}^{\mathrm{T}}(\mathcal{C}\Sigma_{\infty}\mathcal{C}^{\mathrm{T}} + \Sigma_w)^{-1}\mathcal{C}\Sigma_{\infty}\mathcal{A}^{\mathrm{T}}. \tag{33}$$

The controller is applied in real time by computing, at iteration $k$,

$$\hat{\boldsymbol{x}}_{k|k} = \hat{\boldsymbol{x}}_{k|k-1} + \mathscr{H}_{\infty}(\boldsymbol{s}_k - \mathcal{C}\hat{\boldsymbol{x}}_{k|k-1} + \mathcal{D}\boldsymbol{u}_k), \tag{34a}$$

$$\hat{\boldsymbol{x}}_{k+1|k} = \mathcal{A}\hat{\boldsymbol{x}}_{k|k} + \mathcal{B}\boldsymbol{u}_k, \tag{34b}$$

$$\boldsymbol{u}_k = \langle \hat{\boldsymbol{\varphi}} \rangle_{k+1|k} = \mathbf{P}_{\mu 2 \varphi}\mathbf{M}_{\mu}\hat{\boldsymbol{x}}_{k+1|k}, \tag{34c}$$

where the hat represents conditional mean estimation of the state $\boldsymbol{x}$.

### D. Upsampled Commands to the LGS Frame Rate

LGS-MCAO systems use intrinsically two frame rates: one for the NGS and another for the LGS loop. The latter is always faster and determines the commands update rate. Such is the case of NFIRAOS, where the LGS loop is driven at a fixed 800 Hz frame rate.

One thus is interested in obtaining the commands

$$u^{\mathrm{opt}}_{k+j/n} = \langle \hat{\boldsymbol{\varphi}} \rangle_{k+j/n|k} = \mathbf{P}_{\mu 2 \varphi} \langle \hat{\boldsymbol{\mu}} \rangle_{k+j/n|k}, \tag{35}$$

where $n = T_s/T_{\mathrm{lgs}}$ is an integer ratio of the coarse and fine sampling times.

The upsampled estimates $\langle \hat{\boldsymbol{\varphi}} \rangle_{k+j/n|k}$ are easily obtained by discretizing the continuous model of Eq. (27) using $T_{\mathrm{lgs}}$ instead of $T_s$. It follows (for a single controlled mode $i$)

$$\begin{aligned} \langle \boldsymbol{\mu}_i \rangle^{\mathrm{opt}}_{k+j/n} &= (\mathbf{K}_j)_i \hat{\mathbf{x}}_{k|k} \\ &= [\Xi_{\mathrm{lgs}}(\mathcal{A}_{T_{\mathrm{lgs}}})^j]_i (\mathbf{M}_d)_i \hat{\mathbf{x}}_{k|k}, \qquad j \in \{0, \cdots, n-1\}, \end{aligned} \tag{36}$$

where $\mathcal{A}_{T_{\text{lgs}}} \triangleq e^{A_{T_{\text{lgs}}}}$ and $\Xi_{T_{\text{lgs}}} = (1/T_{\text{lgs}})C(e^{A_{T_{\text{lgs}}}} - I)(A)^{-1}$ and $(\mathbf{M}_{\text{d}})_i$ is a 0–1 valued matrix that extracts the $d_{1,k}$, $d_{2,k}$ components for mode $i$.

Concatenating modes, one can therefore obtain an all-at-once optimal command by setting

$$\langle \mu \rangle_{k+j/n}^{\text{opt}} = \mathbf{K}_j \hat{\boldsymbol{x}}_{k|k} = \mathbf{U}_j \mathbf{M}_d \hat{\boldsymbol{x}}_{k|k}, \qquad j \in \{0, \cdots, n-1\}, \tag{37}$$

where $\mathbf{U}_j \in \Re^{6\times 2}$ concatenates matrices $[\Xi_{\text{lgs}}(\mathcal{A}_{T_{\text{lgs}}})^j]_i$ for all six NGS modes:

$$\mathbf{U}_j \triangleq \begin{pmatrix} [\Xi_{\text{lgs}}(\mathcal{A}_{T_{\text{lgs}}})^j]_1 \\ \cdots \\ [\Xi_{\text{lgs}}(\mathcal{A}_{T_{\text{lgs}}})^j]_6 \end{pmatrix}. \tag{38}$$

The average upsampled estimated mode disturbance is given by (for any given NGS mode)

$$\frac{\Xi_{T_{\text{lgs}}}}{n} \sum_{j=0}^{n-1} (\mathcal{A}_{T_{\text{lgs}}})^j = \frac{\Xi_{T_{\text{lgs}}}}{n} \sum_{j=0}^{n-1} (e^{AT_{\text{lgs}}})^j. \tag{39}$$

Taking limits leads to

$$\lim_{n\to+\infty} \frac{\Xi_{T_{\text{lgs}}}}{n} \sum_{i=0}^{n-1} (e^{AT_{\text{lgs}}})^i = \frac{1}{T_s} \int_0^{T_s} e^{At} \mathrm{d}t \tag{40}$$

$$= \frac{1}{T_s} C(e^{AT_s} - I)A^{-1} \tag{41}$$

$$= \Xi, \tag{42}$$

thus providing the average over $T_s$ as the average of averages over $T_{\text{lgs}}$; note that $\Xi_{\text{lgs}} \to 1$ when $n \to \infty$ (since $T_{\text{lgs}} \to 0$).

Since the estimation step remains exactly the same as before, there is no change to the coarse-grain state space nor to the Kalman filter. In other words, the optimal controller runs at the WFS's sampling frequency. This is particularly attractive from the real-time computation point of view. The only difference is with the measurements, where now the effect of the controls on the residual WF needs to be accurately removed due to intersample actuation to produce what is commonly called *pseudo-open-loop measurements* $\boldsymbol{s}_k^{\text{ol}} = \mathbf{G}\langle\phi\rangle_k = \mathbf{G}(\langle\phi^{\text{res}}\rangle_k + \langle\phi^{\text{dm}}\rangle_k)$. Thus, the model is that of Eqs. (26)–(31) with $\mathcal{D} \triangleq 0$ to remove the intersample fed-back commands from the measurements.

A similar development is presented in [30] when dealing with vibration suppression algorithms for this class of MCAO systems.

The operations to be executed in real time are now [compare to Eq. (34)]

$$\hat{\boldsymbol{x}}_{k|k} = \hat{\boldsymbol{x}}_{k|k-1} + \mathscr{H}_\infty(\boldsymbol{s}_k^{\text{ol}} - \mathcal{C}\hat{\boldsymbol{x}}_{k|k-1}), \tag{43a}$$

$$\hat{\boldsymbol{x}}_{k+1|k} = \mathcal{A}\hat{\boldsymbol{x}}_{k|k} + \mathcal{B}\boldsymbol{u}_k, \tag{43b}$$

$$\boldsymbol{u}_{k+j/n} = \mathbf{P}_{\mu 2\varphi} \mathbf{U}_j \mathbf{M}_d \hat{\boldsymbol{x}}_{k|k}, \tag{43c}$$

with the pseudo-open-loop measurement given by

$$\boldsymbol{s}_k^{\text{ol}} = \boldsymbol{s}_k + \mathbf{G}\mathbf{N}\frac{1}{n}\sum_{j=0}^{n-1} \boldsymbol{u}_{k-1+j/n}. \tag{44}$$

Figure 2 depicts an example of temporal trajectories for the six NGS modes, using the *zero-order-hold* commands and the upsampled commands presented above.

### 1. Model Identification

Model identification is treated in [28,29], with the mode-by-mode $\mathcal{A}$ matrices identified by fitting the first few steps of a second-order model to the autocorrelation of the modes (computed from the temporal PSDs assuming frozen flow with the Wiener–Khinchin theorem). State-noise covariance matrices are determined from the solution of discrete-time Lyapunov equations that defines the state covariance noise from a linear model and the total disturbance of each mode (computed from analytical expressions in [31] and compared to the numerical integration of the temporal PSDs).

### 2. Use of Multiple Frame Rates

One could arguably point out that in order to further optimize the NGS loop one should pick one frame rate per OIWFS and combine optimally the available information at each time step, as is explained in [32] for the NGS/LGS case. However, the lack of sufficient measurement redundancy renders the reconstruction rank-deficient when only using measurements from a reduced set of OIWFS [23]. Until a full set of measurements is available, providing three independent TT measurements in the field, the reconstruction and control degrade in such a way that a common frame rate appears to be the best one can do.

Simulations show that since the NGS modes are spatially uncorrelated, uncorrelated between layers, and temporally considered uncorrelated (and furthermore have similar variances and temporal spectra), the estimate produced from a reduced set using multirate can always be outperformed by

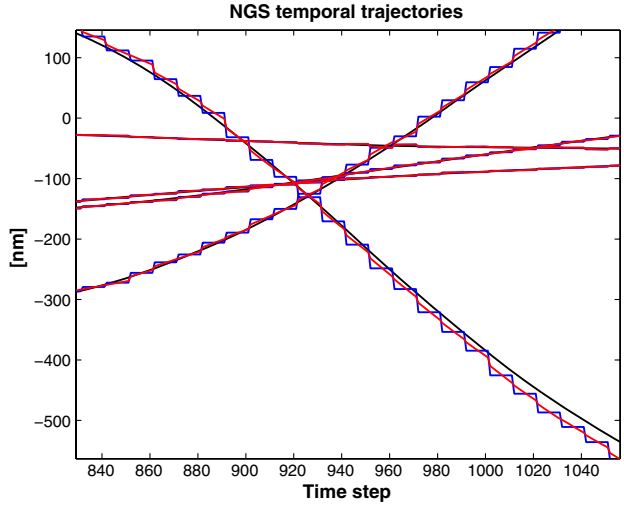


Fig. 2. (Color online) Time series comparison between the zoh MV commands and the upsampled commands based on the internal model, $T_s = 11/800$ s (upsampling factor of 11). Black, disturbance trajectories; blue, zoh MV commands; red, upsampled MV commands. The five families of curves are for the five Zernike polynomials in the telescope pupil.

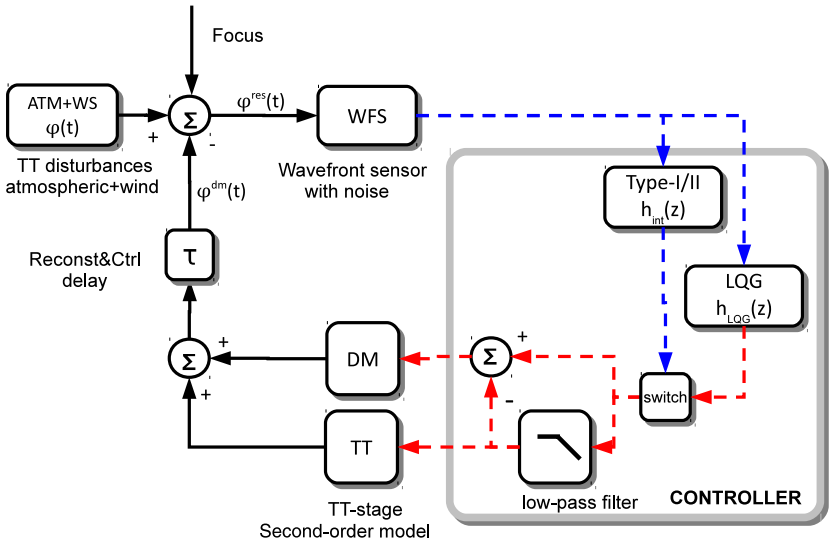


Fig. 3. (Color online) NGS loop block diagram. Block *switch* is also responsible for *zero-order holding* the signals from the integrator controllers to the highest 800 Hz frame rate of the high-order LGS loop (dashed red lines). Focus mode is controlled via a focus blending loop (not shown) combining a trombone for slow refocusing and the DM for the remainder. Continuous black lines, continuous time; blue dashed lines, NGS loop frame rate. The focus mode is controlled at the same frame rate as the TT and TA modes.

choosing a common frequency for all the OIWFS and using a more straightforward single-rate LQG controller.

## 4. SAMPLE NUMERICAL RESULTS

### A. Loop Description and Simulation Parameters

Only the low-order NGS loop is simulated in what follows, as it is the chief driver of sky-coverage estimates. The high-order LGS loop is not taken into account at this stage, and, under the AHST scheme, the NGS and LGS loops are decoupled (see block diagram in Fig. 3). A postprocessing technique to evaluate sky coverage without the need to run fully integrated simulations has been demonstrated by Wang *et al.* [21].

A custom code was written to compare the NGS loop performance using integrator-based controllers (single and double integrators) to the MV solution. The former were optimized using a fast minimization procedure for the three double-integrator parameters, i.e., the controller gain, 0 dB cross frequency, and phase margin [33]. For all the configurations tested (i.e., noise level, sampling frequency, and gain range), the residual disturbance criterion used is convex (empirical observation, left unproved), allowing the combination of fast methods to find the global minimum under a 45 deg imposed phase margin followed by further reoptimizing the phase margin and gain around the working point found previously.

Table 1 summarizes the parameters used in the simulation. The WFS noise values are equivalent to those of an H-band star with magnitudes 13 and 20, sampled at 800 and 20 Hz, respectively, which covers a broad range of NGS stars used for WF sensing in a TMT-NFIRAOS-like configuration. Noise is computed assuming an SR variation across the 2 arc min patrol FoV from 0.5 to 0.1 at the edge in the H-band. Total throughput is 0.3, a rather small value chosen to boost overall noise to compensate for aliasing and implementation errors that are not in the simulation but are considered in the full-featured sky-coverage simulations.

Figure 4 depicts sample temporal PSDs, corresponding to the 50th-percentile observing conditions expected at TMT with wind shake added to one of the tip or tilt modes [34]. The integrated total WF error is given in Table 1.

The TT temporal correction split is based on a temporal filtering approach where the TT stage corrects for low-frequency large-amplitude TT disturbances and the ground DM corrects for its complement. This approach has been

**Table 1. Parameters Used in the End-to-End Monte Carlo Numerical Simulations[a]**

| | | |
|---|---|---|
| Disturbances | Atmospheric | $\sigma_{TT} = 603$ nm rms<br>$\sigma_{TA} = 407$ nm rms<br>$L_0 = 30$ m<br>$r_0$@0.5 μm = 0.186 m |
| | Wind shake (50% ile) | $\sigma_{WS} = 7.5$ mas rms (single TT axis) |
| | Sodium-range focus | $\sigma_F = 505$ nm rms |
| WFS | Type | Modal |
| | No. WFSs | 3<br>Two single-aperture TTs and one $2 \times 2$ |
| | Frame rates | $\{16, \cdots, 800\}$ Hz |
| | Read + detector noise | On |
| Controllers | Type I | Optimized gain integrator |
| | Type II | Optimized double integrator |
| | MV | w/second-order disturbance models |
| | Servo-lag | 1 ms |
| Correctors | Type | Modal |
| | Frame rate | $\{16, \cdots, 800\}$ Hz |
| | TT mount | Second-order model, 90 Hz bandwidth (–3 dB) |
| | No. DMs | 2, infinite bandwidth |
| Simulation | Duration | 30 s |
| | No. modes | 6 (2 TT, 3 TA, focus) |
| | NGS field diameter | 2 arc min |
| | Mode of operation | MCAO |
| | Wavelength | $\lambda_{WFS} = 1.65$ μm |

[a]The TT/TA and focus disturbance PSDs are depicted in Fig. 4.

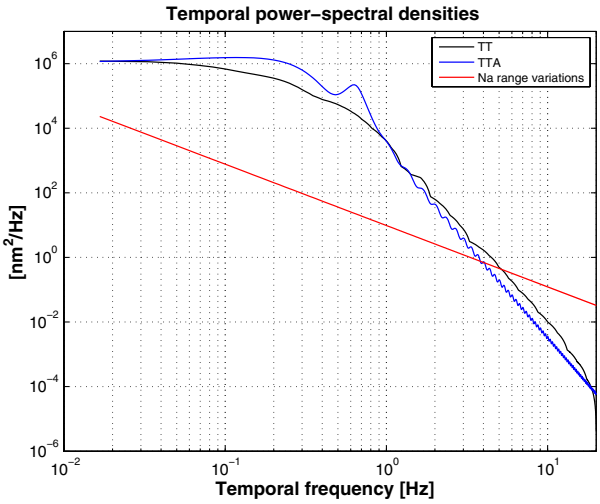


Fig. 4. (Color online) NGS mode PSDs. TT use standard formulae for a 30 m telescope with 30 m outer scale and median 18.6 cm Fried coherence length. To it is added wind buffeting (from finite-element analysis of TMT) with 7.5 mas rms on a single axis. TA PSDs were obtained with the formulation given in [21]. The focus error PSD follows $\propto f^{-1.97} \approx f^{-2}$ [25], excluding low-temporal filtering from the trombone and matched-filtering update.

extensively studied and compared to the optimal MV solution for the woofer–tweeter temporal split presented in [33]. The simpler *ad hoc* solution provides the same performance as the full-featured MV solution and is more robust with respect to loop delays not fully taken into account in the optimal woofer–tweeter analysis.

In order to cope with the limited −3 dB bandwidth of roughly 90 Hz, a cutoff frequency $f_c = 20$ Hz is assigned to the low-pass filter.

Results are computed assuming the NGS wavelength in the J-band using an optimal frame rate computed on an asterism-per-asterism basis and averaged over 30 s of equivalent real-time simulation (excluding the initial transient period).

### B. Sky-Coverage Comparison

Figure 5 plots the sky coverage (given by the cumulative probability following the definition in Section 1) obtained over 500 representative asterisms [8] as a function of the WF residual, and averaged over all cases for a given frame rate (optimized on a case-by-case basis). For a given sky-coverage probability the MV provides smaller residuals, or, likewise, for a fixed residual the MV increases the probability of finding a suitable asterism for guiding.

Table 2 summarizes the results obtained and further specifies the TT residual only. As a first comment, the comparison of the theoretical residual values (based on discrete-time transfer functions) underestimates the actual values obtained in the full simulation. Though the discrepancy is not outstanding, this effect is particularly observed in the low-temporal sampling frequency range.

Initial results were presented in [28] for the five NGS modes only, i.e., no focus error due to sodium-range variations. The main motivation of that paper was optimization of the integrator-based controllers. Results showed the same trend as those obtained for the six-NGS-mode case but were incomplete. Furthermore, the upsampled MV controller presented here was not assessed at the time.

Over all the cases tested, an estimated 4.8 nm rms improvement (in quadrature) is obtained with the single-rate MV controller with command upsampling with respect to the MV controller with "zoh" commands. Compared to the integrator-based controllers, an improvement of 21 and 38.5 nm rms, respectively, to the type-II and type-I controllers is found.

Figure 6 depicts three asterisms giving the worst, median, and best performances. Note the worst asterism consists in a single NGS star, located at the limit of the 2 arc min patrol FoV. Out of the total of ∼500 asterism set, there are 38 cases with only two NGSs and 15 cases with one NGS.

The histogram of frame rates in Fig. 7 shows the MV controllers more often using frame rates closer to their respective medians. Also, the MV tends to use less the upper end of frame rates, certainly a sign of (a) the temporal prediction partially recovering the temporal lag error of lower frame rates and

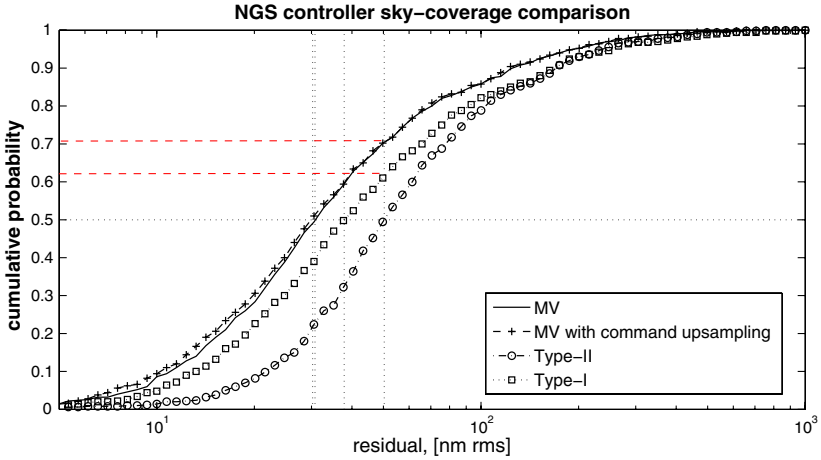


Fig. 5. (Color online) Sky-coverage comparison (cumulative probability density function). Curves represent the cumulative probability of finding one asterism suitable for the NGS WF sensing as a function of the residual WF; see definition of *sky coverage* in Section 1. Vertical dotted lines indicate the residuals in nanometer rms obtained for the median case. The MV delivers roughly 30 nm rms, the type-II delivers slightly below 40 nm rms, and finally the type-I delivers ∼50 nm rms. The red dashed lines indicate the increase in sky coverage expected from the MV with a gain of 10% and 20% when compared to the type-II and type-I controllers, respectively.

**Table 2. Results in Nanometer RMS[a]**

| Median | | | | | | |
|---|---|---|---|---|---|---|
| | Type I | Type II | MV | MV Up | Th. Type I | Th. Type II |
| All modes | 50.3 | 37.8 | 30.6 | 29.6 | 44.4 | 32.1 |
| TT only | 47.4 | 35.1 | 26.2 | 25.4 | | |
| **Average** | | | | | | |
| | Type I | Type II | MV | MV Up | Th. Type I | Th. Type II |
| All modes | 117.1 | 124.1 | 91.1 | 91.2 | 106.3 | 109.4 |
| TT only | 111.0 | 117.1 | 83.2 | 83.2 | | |

[a]Top table with median results and bottom with average results. The last two columns refer to theoretical results using a transfer-function approach.

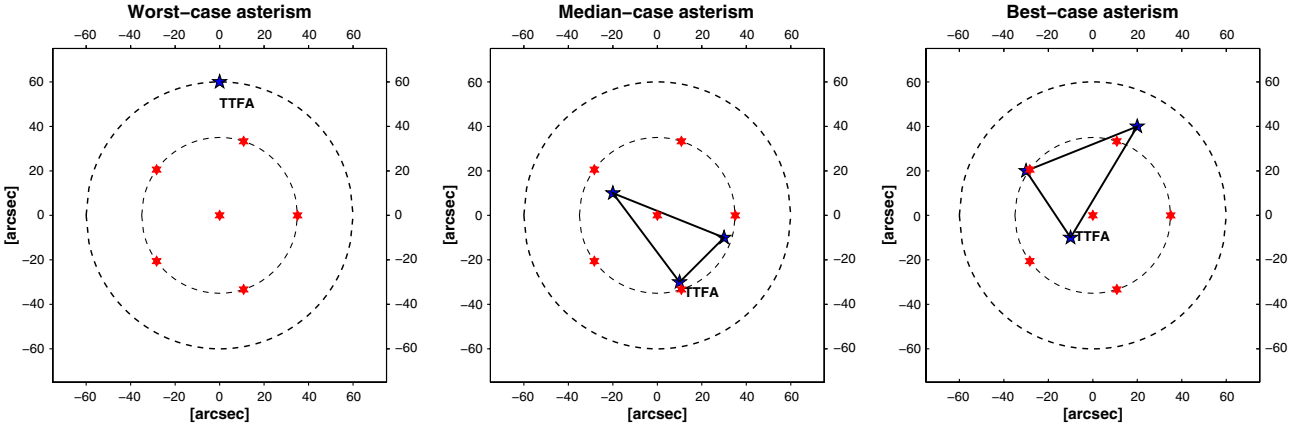


Fig. 6. (Color online) Sample of asterisms for the worst-, median-, and best-case scenarios. The star used for TTFA is indicated. The LGS 35 arc sec radius pentagon is overplotted (red stars) for convenience.

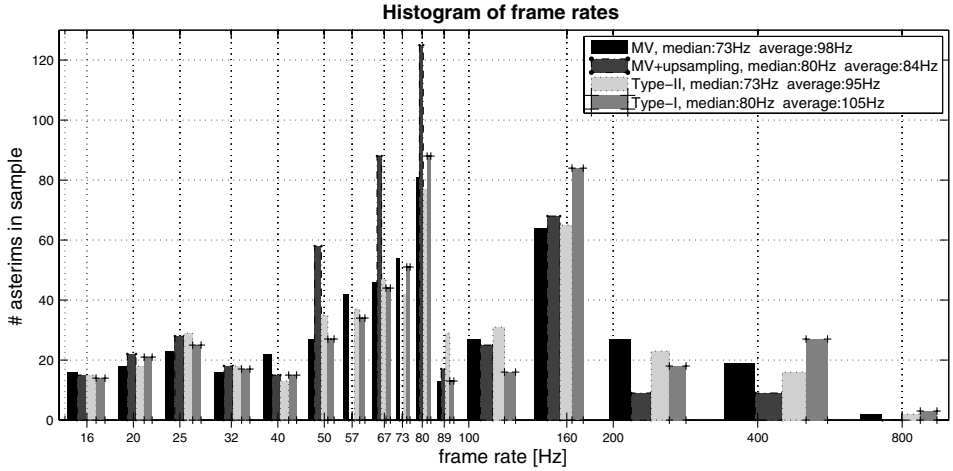


Fig. 7. Histogram of frame rates required by the different controllers. Median and average values indicated in the legend. The MV controller presents more clustered median and average values.

(b) the 1.25 ms loop delay not taken into account in the LQG analysis, creating a model/system mismatch to which the overall performance is sensitive, particularly when the NGS sampling rate approaches the LGS rate.

## 5. CONCLUSION

This paper presents the design of an MV controller for TT and TA modes arising in LGS-based MCAO, which often needs to be sensed at low frame rates for faint NGSs. A further extension also proposed here consists of optimally upsampling the correction of these errors to the LGS frame rate, the NGS controller being updated at a lower frame rate.

Using end-to-end temporal numerical simulations for the median case (TMT conditions) with 500 different asterisms, it is shown the MV controllers outperform the more traditional suboptimal integrator-based controllers, by ~21 nm rms in quadrature (optimized double integrator) and ~38.5 nm rms

(optimized single integrator). Higher gains are specially obtained for faint asterisms (with frame rates as low as 16 Hz) and even when fewer than three NGSs are available for guiding.

Following the sky-coverage definition assumed in this paper, the MV further increases by ∼10% and ∼20% the sky coverage level obtained with a type-II or a type-I controller, respectively. These results will now be thoroughly confirmed with TMT's high-fidelity sky-coverage simulator, which includes both LGS and NGS loops.

The advantages of the MV are manifold. Although conceptually more complex, it is much faster to compute offline, vibration suppression can be easily embedded, it supports upsampling of commands to the LGS loop frame rate (800 Hz for NFIRAOS), and it is directly optimized in discrete time [33].

In the future, this model will be expanded to accommodate more modes to comply with the *MVST* [21], which provides a better joint estimate of NGS + LGS modes.

## APPENDIX A: STATE-NOISE MODELING

A rigorous and thorough treatment of the discretization of the continuous-time state-space stochastic can be found in [35], Section 4.5 and previous.

Start from the stochastic model

$$\dot{\boldsymbol{x}} = A_c \boldsymbol{x} + \boldsymbol{v}^c, \tag{A1}$$

where $\boldsymbol{v}^c$ is a continuous white noise with covariance function $r_v(t) = \Sigma_v^c \delta(t)$, and $\delta(t)$ is the Dirac delta function.

The discrete-time model that has $\boldsymbol{x}_k = \boldsymbol{x}(t = kT)$ is given by

$$\boldsymbol{x}_{k+1} = e^{A_c T} \boldsymbol{x}_k + \int_{kT}^{(k+1)T} e^{A_c((k+1)T-t)} \boldsymbol{v}^c(t) \mathrm{d}t \triangleq e^{A_c T} \boldsymbol{x}_k + \boldsymbol{v}_k^d. \tag{A2}$$

The covariance of the discrete-time noise is given by

$$\Sigma_v^d = \mathrm{VAR}\left( \int_{kT}^{(k+1)T} e^{A_c((k+1)T-t)} \boldsymbol{v}^c(t) \mathrm{d}t \right) = \int_0^T e^{A_c t} \Sigma_v^c e^{A_c^{\mathrm{T}} t} \mathrm{d}t. \tag{A3}$$

In order to evaluate this integral, proceed by noting that the solution to the algebraic continuous-time Lyapunov equation

$$A_c \bar{\Sigma} + \bar{\Sigma} A_c^{\mathrm{T}} + \Sigma_v^c = 0, \tag{A4}$$

is given by

$$\bar{\Sigma} = \int_0^{+\infty} e^{A_c t} \Sigma_v^c e^{A_c^{\mathrm{T}} t} \mathrm{d}t. \tag{A5}$$

The solution to Eq. (A3) is given by

$$\begin{aligned} \int_0^T e^{A_c t} \Sigma_v^c e^{A_c^{\mathrm{T}} t} \mathrm{d}t &= \int_0^{+\infty} e^{A_c t} \Sigma_v^c e^{A_c^{\mathrm{T}} t} \mathrm{d}t - \int_T^{+\infty} e^{A_c t} \Sigma_v^c e^{A_c^{\mathrm{T}} t} \mathrm{d}t \\ &= \bar{\Sigma} - e^{-TA_c} \bar{\Sigma} e^{-TA_c^{\mathrm{T}}}, \end{aligned} \tag{A6}$$

which is a discrete-time Lyapunov equation. In practice, the presence of the integral variable on the state will make the computation of $\bar{\Sigma} = \infty$. To circumvent this, numerical integration of the differential continuous-time Lyapunov equation can be used.

## ACKNOWLEDGMENTS

The authors thank Caroline Kulcsár and Henri-François Raynaud for fruitful discussions regarding the upsampled MV controller.

## REFERENCES

1. F. Roddier, *Adaptive Optics in Astronomy* (Cambridge University, 1999).
2. J. W. Hardy, *Adaptive Optics for Astronomical Telescopes* (Oxford University, 1998).
3. J. M. Beckers, "Increasing the size of the isoplanatic patch with multiconjugate adaptive optics," in *Proceedings of the ESO Conference on Very Large Telescopes and Their Instrumentation* (ESO, 1988), Vol. **2**, pp. 693–703.
4. T. Fusco, J.-M. Conan, G. Rousset, L. M. Mugnier, and V. Michau, "Optimal wave-front reconstruction strategies for multiconjugate adaptive optics," J. Opt. Soc. Am. A **18**, 2527–2538 (2001).
5. J. Herrmann, "Phase variance and Strehl ratio in adaptive optics," J. Opt. Soc. Am. A **9**, 2257–2258 (1992).
6. E. Marchetti, R. Brast, B. Delabre, R. Donaldson, E. Fedrigo, C. Frank, N. Hubin, J. Kolb, J.-L. Lizon, M. Marchesi, S. Oberti, R. Reiss, C. Soenke, S. Tordo, A. Baruffolo, P. Bagnara, A. Amorim, and J. Lima, "MAD on sky results in star oriented mode," Proc. SPIE **7015**, 70150F (2008).
7. R. C. Flicker, F. J. Rigaut, and B. L. Ellerbroek, "Tilt anisoplanatism in laser-guide-star-based multiconjugate adaptive optics. Reconstruction of the long exposure point spread function from control loop data," Astron. Astrophys. **400**, 1199–1207 (2003).
8. L. Wang, D. Andersen, and B. Ellerbroek, "Sky coverage modeling for the whole sky for laser guide star multiconjugate adaptive optics," Appl. Opt. **51**, 3692–3700 (2012).
9. R. M. Clare, B. L. Ellerbroek, G. Herriot, and J.-P. Véran, "Adaptive optics sky coverage modeling for extremely large telescopes," Appl. Opt. **45**, 8964–8978 (2006).
10. R. M. Clare and B. L. Ellerbroek, "Sky coverage estimates for adaptive optics systems from computations in Zernike space," J. Opt. Soc. Am. A **23**, 418–426 (2006).
11. B. Neichel, F. Rigaut, A. Serio, G. Arriagada, M. Boccas, C. d'Orgeville, V. Fesquet, C. Trujillo, W. N. Rambold, R. L. Galvez, G. Gausachs, T. B. Vucina, V. Montes, C. Urrutia, C. Moreno, S. J. Diggs, C. Araya, J. Lührs, G. Trancho, M. Bec, C. Marchant, F. Collao, E. Carrasco, M. Edwards, P. Pessev, A. Lopez, and H. Diaz, "Science readiness of the Gemini MCAO system: GeMS," Proc. SPIE **8447**, 84474Q (2012).
12. F. Rigaut, B. Neichel, M. Boccas, C. d'Orgeville, G. Arriagada, V. Fesquet, S. J. Diggs, C. Marchant, G. Gausach, W. N. Rambold, J. Luhrs, S. Walker, E. R. Carrasco-Damele, M. L. Edwards, P. Pessev, R. L. Galvez, T. B. Vucina, C. Araya, A. Gutierrez, A. W. Ebbers, A. Serio, C. Moreno, C. Urrutia, R. Rogers, R. Rojas, C. Trujillo, B. Miller, D. A. Simons, A. Lopez, V. Montes, H. Diaz, F. Daruich, F. Colazo, M. Bec, G. Trancho, M. Sheehan, P. McGregor, P. J. Young, M. C. Doolan, J. van Harmelen, B. L. Ellerbroek, D. Gratadour, and A. Garcia-Rissmann, "Gems: first on-sky results," Proc SPIE **8447**, 84470I (2012).
13. S. D'Odorico, S. Ramsay, N. Hubin, J. C. Gonzales, and F. M. Zerbi, "An introduction to the E-ELT instrumentation and post-focal adaptive optics module studies," ESO Messenger **140**, 17 (2010).
14. B. L. Ellerbroek, S. M. Adkins, D. R. Andersen, J. Atwood, A. Bastard, Y. Bo, M.-A. Boucher, C. Boyer, P. W. G. Byrnes, K. Caputa, S. Chen, C. Correia, R. Cousty, J. T. Fitzsimmons, L. Gilles, J. Gregory, G. Herriot, P. Hickson, A. Hill, J. Pazder, H. Pagès, T. Pfrommer, V. A. Reshetov, S. Roberts, J.-C. Sinquin, M. Schoeck, M. Smith, J.-P. Véran, L. Wang, K. Wei, and I. Wevers, "TMT adaptive optics program status report," Proc. SPIE **8447**, 84471J (2012).
15. G. Herriot, D. Andersen, J. Atwood, P. Byrnes, M.-A. Boucher, C. Boyer, K. Caputa, C. Correia, J. Dunn, B. Ellerbroek, J.

Fitzsimmons, L. Gilles, P. Hickson, A. Hill, D. Kerley, J. Pazder, V. Reshetov, S. Roberts, M. Smith, J.-P. Véran, L. Wang, and I. Wevers, "TMT NFIRAOS: adaptive optics system for the thirty meter telescope," Proc. SPIE **8447**, 84471M (2012).
16. M. Lloyd-Hart, R. Angel, N. M. Milton, M. Rademacher, and J. Codona, "Design of the adaptive optics systems for GMT," Proc. SPIE **6272**, 62720E (2006).
17. E. J. Barton, J. E. Larkin, A. M. Moore, S. A. Wright, D. Crampton, L. Simard, B. Macintosh, P. Côté, A. J. Barth, A. M. Ghez, J. R. Lu, T. J. Davidge, and D. R. Law, "The infrared imaging spectrograph (IRIS) for TMT: the science case," Proc. SPIE **7735**, 77355M (2010).
18. L. Wang, B. Ellerbroek, and J. P. Veran, "High fidelity sky coverage analysis via time domain adaptive optics simulations," Appl. Opt. **48**, 5076–5087 (2009).
19. L. Gilles and B. L. Ellerbroek, "Split atmospheric tomography using laser and natural guide stars," J. Opt. Soc. Am. A **25**, 2427–2435 (2008).
20. L. Gilles, L. Wang, and B. L. Ellerbroek, "Minimum variance split tomography for laser guide star adaptive optics," Eur. J. Control **17**, 327–334 (2011).
21. L. Wang, L. Gilles, and B. Ellerbroek, "Analysis of the improvement in sky coverage for multiconjugate adaptive optics systems obtained using minimum variance split tomography," Appl. Opt. **50**, 3000–3010 (2011).
22. J.-P. Véran and G. Herriot, "Type II woofer–tweeter control for NFIRAOS on TMT," in *Adaptive Optics: Methods, Analysis and Applications* (Optical Society of America, 2009), p. JTuC2.
23. B. L. Ellerbroek and F. Rigaut, "Methods for correcting tilt anisoplanatism in laser-guide-star-based multiconjugate adaptive optics," J. Opt. Soc. Am. A **18**, 2539–2547 (2001).
24. R. J. Noll, "Zernike polynomials and atmospheric turbulence," J. Opt. Soc. Am. A **66**, 207–211 (1976).
25. T. Pfrommer and P. Hickson, "High-resolution lidar observations of mesospheric sodium and implications for adaptive optics," J. Opt. Soc. Am. A **27**, A97–A105 (2010).
26. R. Ragazzoni, E. Marchetti, and F. Rigaut, "Modal tomography for adaptive optics," Astron. Astrophys. **342**, L53–L56 (1999).
27. L. Lundström and P. Unsbo, "Transformation of Zernike coefficients: scaled, translated, and rotated wavefronts with circular and elliptical pupils," J. Opt. Soc. Am. A **24**, 569–577 (2007).
28. C. Correia, J.-P. Véran, G. Herriot, B. Ellerbroek, L. Wang, and L. Gilles, "Advanced control of low order modes in laser guide star multi-conjugate adaptive optics systems," Proc. SPIE **8447**, 84471S (2012).
29. C. Correia, H.-F. Raynaud, C. Kulcsár, and J.-M. Conan, "On the optimal reconstruction and control of adaptive optical systems with mirror dynamics," J. Opt. Soc. Am. A **27**, 333–349 (2010).
30. C. Correia, J.-P. Véran, and G. Herriot, "Advanced vibration suppression algorithms in adaptive optics systems," J. Opt. Soc. Am. A **29**, 185–194 (2012).
31. D. M. Winker, "Effect of a finite outer scale on the Zernike decomposition of atmospheric optical turbulence," J. Opt. Soc. Am. A **8**, 1568–1573 (1991).
32. C. Kulcsár, H.-F. Raynaud, C. Petit, and J.-M. Conan, "Optimal AO control with NGS/LGS wavefront sensors: the multirate case," Proc. SPIE **7736**, 773614 (2010).
33. C. Correia and J. Véran, "Woofer–tweeter temporal correction split in atmospheric adaptive optics," Opt. Lett. **37**, 3132–3134 (2012).
34. S. G. Els, T. Travouillon, M. Schöck, R. Riddle, W. Skidmore, J. Seguel, E. Bustos, and D. Walker, "Thirty meter telescope site testing VI: turbulence profiles," Publ. Astron. Soc. Pac. **121**, 527–543 (2009).
35. T. Söderström, *Discrete-Time Stochastic Systems, in Advanced Textbooks in Control and Signal Processing* (Springer-Verlag, 2002).